Antonio Iacomini, Sebastiano Garroni, Marzia Mureddu, Luca Malfatti, Swapneel Thakkar, Roberto Orrù, Simone Barbarossa, Ekaterina Pakhomova, Giacomo Cao, Juan Antonio Tamayo-Ramos, Sandra de la Parra, Carlos Rumbo, Álvaro Garcìa, José F. Bartolomé, Lorena Pardo

Processing, microstructure, electrical properties and cytotoxic behaviour of lead-free 0.99K0.5Na0.5NbO3-0.01BiFeO3 piezoceramics prepared using Spark Plasma Sintering (SPS), Journal of Solid State Chemistry Volume 316, December 2022, 123589, ISSN 0022-4596,

The publisher's version is available at:
https://doi.org/10.1016/j.jssc.2022.123589

Processing, microstructure, electrical properties and cytotoxic behaviour of lead-free $0.99K_{0.5}Na_{0.5}NbO_3$-$0.01BiFeO_3$ piezoceramics prepared using Spark Plasma Sintering (SPS)

Antonio Iacomini[1*], Sebastiano Garroni[1], Marzia Mureddu[1], Luca Malfatti[2], Swapneel Thakkar[3], Roberto Orrù[4], Simone Barbarossa[4], Ekaterina Pakhomova[4], Giacomo Cao[4], Juan Antonio Tamayo-Ramos[5], Sandra de la Parra[5], Carlos Rumbo[5], Álvaro Garcìa[6], José F. Bartolomé[6] and Lorena Pardo[6]

[1] *Department of Chemistry, Physics, Mathematics and Natural Sciences, University of Sassari, 07100 Sassari, Italy.*

[2]*Laboratory of Materials Science and Nanotechnology (LMNT), Department of Biomedical Sciences, University of Sassari, CR-INSTM, Viale San Pietro, 07100 Sassari, Italy.*

[3]*CNRS, Institut Charles Sadron, University of Strasbourg, France.*

[4] *Dipartimento di Ingegneria Meccanica, Chimica e dei Materiali, Unità di Ricerca del Consorzio Interuniversitario Nazionale Per la Scienza e Tecnologia dei Materiali, Università degli Studi di Cagliari, via Marengo 2, 09123 Cagliari, Italy.*

[5]*International Research Centre in Critical Raw Materials—ICCRAM, Universidad de Burgos, Plaza Misael Bañuelos s/n, 09001 Burgos, Spain.*

[6] *Instituto de Ciencia de Materiales de Madrid, CSIC, c/Sor Juana Ines de la Cruz, 3 Cantoblanco, 28049 Madrid, Spain.*

****

* Corresponding author: Antonio Iacomini

Phone: + 39 3341840558

E-mail address (corresponding author): aiacomini@uniss.it

Abstract

In this work, "lead free" $0.99K_{0.5}Na_{0.5}NbO_3$-$0.01BiFeO_3$ (KNN-BF) piezoceramics were prepared by a combination of mechanochemical activation, Spark Plasma Sintering and post-annealing treatment. Results show that the annealing treatment causes important microstructural and electrical changes. The SPS sample was characterized by low electrical resistance, while the air annealed samples showed better insulating properties due to a partial compensation of the oxygen vacancy. The best piezoelectric properties were found for the samples annealed at 1000 and 1050 °C for 2h due to the optimum grain size and oxygen vacancy compensation achieved. A further enhancement of the dielectric and piezoelectric properties was achieved through a second annealing treatment in oxygen flux at 1050°C for 30 minutes. Moreover, the toxicity of the pellets was evaluated through exposure experiments to the pulverized KNN-BF pellets, employing two widely used human and environmental cellular models.

Keywords: Potassium sodium niobate, High Energy Ball Milling, Spark Plasma Sintering, Raman spectroscopy, Dielectric, Cytotoxic assessment.

1. Introduction

The versatility and potential complexity of the perovskite-type crystal structure makes it very attractive for the synthesis of materials with intended functionalities.**[1]** Among them, the piezoceramic materials of complex oxides are the object of structural tailoring by the search of solid solution systems with compositionally induced polymorphic phase boundaries.**[2-4]** This aims to get amenable properties for their widespread applications in technological devices ranging from microelectronics, medical diagnostics, sensors and actuators in automobile industry and so on.**[5,6]** In this context, lead-free materials are now the object of an intensive study by the scientific community due to their promising properties which can be compared with some of the most exploited PZT systems. Potassium sodium niobate $K_{0.5}Na_{0.5}NbO_3$ (KNN) is one of the most promising lead-free systems with good dielectric and piezoelectric properties and a high Curie temperature (420°C).**[7-9]** However, it suffers of the high volatility of the alkaline ions at the common sintering temperature (>1100°C). This leads to the deviation from stoichiometry and formation of secondary and undesired phases, low reproducibility, difficulty to obtain high dense product and, obviously, piezo properties still far from PZT systems. To overcome some of these barriers, doping agents, as bismuth ferrite ($BiFeO_3$; BF), can be included in the KNN matrix through a combination of High Energy Ball Milling and sintering process.**[10]** The Spark Plasma Sintering (SPS) is a sintering technique which allows to obtain highly dense piezoceramics in a very short time and using relatively low sintering temperatures.**[11,12]** This technique is particularly attractive for KNN and KNN-based ceramics. However, due to the drastic conditions of the SPS process (high heating rate, high mechanical load, low oxygen partial pressure conditions etc…) the resulting ceramic is generally characterized by inhomogeneity of the bulk composition (especially in the case of complex compositions), small grain size and structural defects, like oxygen vacancy. In particular, the latter are responsible for the conductivity found in "fresh" SPS samples.**[13]** For these reasons, an air annealing treatment is usually necessary in order to increase the size of grains and to decrease the oxygen vacancy concentration. Zhen et al. pointed out the importance of this treatment which obviously affects the piezoelectric properties of the ceramics.**[14]** They found

that for Li and Ta co-doped KNN, the optimal annealing treatment seems to be around 1050°C by using a standard air-treatment, which increased the charge piezoelectric coefficient d_{33} from 162 in the best ceramic by SPS, to 225 pC/N. Monot-Laffez et al. also employed a post annealing treatment in an oxygen flow which appears to be very effective at improving the planar electromechanical coupling factor (k_p) up to 50% for Ta-doped KNN and 60% when using a special synthesis route to improve compositional homogeneity.**[15]** However, the effect of post annealing treatment in the BF-doped KNN system has not previously been reported.

Good electromechanical properties are necessary but not sufficient conditions in medical applications for a lead-free system to be considered alternative to the current lead-based counterpart, inasmuch the composition must also be non-cytotoxic. In literature there are many high performance KNN systems modified with various ions, including antimony for example, whose toxicity is well known.**[16]**

In the light of these considerations, this work is focused on the optimization of the processing, by High Energy Ball Milling and SPS technique, of the pseudo binary solid solution with nominal composition of $0.99K_{0.5}Na_{0.5}NbO_3$-$0.01BiFeO_3$ (KNN-BF). The influence of the post annealing treatments on structure, microstructure, dielectric, electromechanical and cytotoxic behaviour was investigated.

2. Experimental methods

The processing of powders involves a mechanochemical activation method to assists the synthesis of the perovskite, following the same procedure as described in our previous work.**[10]** Sintering experiments were conducted in vacuum using SPS equipment (515S model, Fuji Electronic Industrial Co., Ltd., Kanagawa, Japan) under the following conditions: dwell temperature (T_D), heating rate, dwell time (t_D), and mechanical pressure (P) of 940 °C, 100 °C/min, 5 min, and 50 MPa, respectively. The temperature was measured using a K thermocouple placed inside the diameter die. After sintering, four different samples, named SA2, SA3, SA4 and SA5, were annealed in air for 2 hours respectively at 950, 1000, 1050 and 1100°C, using a heating rate of 4°C/min and a cooling rate of 10°C/min. The

as-sintered SPS sample was named SA1. In order to observe the effect of the different annealing atmosphere on the dielectric and piezoelectric properties of the specimens under study, two more samples were prepared in an oxygen flow atmosphere (flow rate of 100 cm^3/min), called SO1 and SO2. SO1 was annealed in oxygen flow at 1050 ºC for 2h, while SO2 is the sample already annealed in air at 1000°C (SA3) which has undergone a second annealing treatment in oxygen flow at 1050°C for 30 min.

Bulk densities were measured with the Archimedes' method as an average of four measurements. Structural investigations were conducted using a SMARTLAB diffractometer with a rotating anode source of copper (λ=1.54178 Å) working at 40 kV and 100 mA. The patterns were collected in the angular range from 18° to 110° with a step size of 0.05° and a fixed counting time of 15 seconds per point. Microstructure and morphology of the samples have been characterized by Quanta FEI 200 Scanning Electron Microscope. Raman analyses were performed by a Senterra confocal Raman microscope (Bruker) with a 632 nm laser excitation, 1 mW power, and 10× objective.

To measure electric properties, pellets of 14.5 mm diameter were reduced in thickness by polishing down to a thickness of about 1mm. Silver paste was attached on both surfaces of the thin disks, which were then sintered at 400°C for 1 hour. After that, samples were poled in thickness under 20 kV/cm at 50-100°C (depending on the annealing treatment) for 15 minutes in a silicone oil bath, followed by field cooling (FC). Permittivity vs. temperature curves at frequencies from 1 kHz to 1 MHz were measured using an impedance analyser (HP 4194A) from room temperature to 420 °C. The quasi-static d_{33} piezoelectric charge coefficient was measured two hours after poling with a Berlincourt d_{33}-meter at 100Hz. Complex impedance as a function of the frequency was measured with an impedance analyser (HP 4192A-LF) at the radial extensional resonance of the thickness poled thin disks. An automatic iterative method was used in the analysis of the impedance curves to determine the complex electromechanical, elastic and dielectric properties of the ceramics.**[17,18]**

The toxicological potential of the prepared samples was determined by *in vitro* screening employing two model organisms that were selected as representatives of human (A549 cell line) and

environmental exposures (*Saccharomyces cerevisiae*), as described in detail elsewhere.**[19]** The materials under study (SA1, SA2, SA3, SA4 and SA5) and the PZT (commercial reference sample, Meggit Ferroperm PZ26) were smashed in a mortar and sieved (0.125 mm mesh size) to obtain a uniform powder. Stocks of the powder materials resuspended in water at 10 g/L were prepared to carry out the experiments. Before performing the tests, samples were vortexed at full speed and then submitted to ultrasonication for 20 min at low power intensity. Finally, before preparing the different concentrations used in the experiments, samples were vortexed again. Statistical differences were analysed using Prism 8.0.2 (GraphPad Prism, GraphPad Software, Inc.), performing the one-way analysis of variance (ANOVA), followed by Dunnett *post hoc* test to make comparisons between every mean and the control. Differences were considered significant at $P \leq 0.05$.

3. Results and discussion

3.1 Structural and microstructural characterisation

In **Figure 1** is reported the temperature time profile imposed during the sintering process along with the corresponding sample displacement. Two main phenomena can be recognized, which have been indicated as T1 and T2. The first shrinkage (T1) of about 0.8 mm occurs during the first minutes of the SPS run, and is due to the particle rearrangement following the application of the mechanical load (50 MPa). The second phenomenon (T2), which starts at around 320°C and it is completed at around 925°C, is due to the sintering process which causes an overall displacement of about 3.3 mm. The densification is completed just before the desired sintering temperatures (940°C) is reached, while during the isotherm no more shrinkage is observed. In **Figure 2** are reported the photographs of the sintered pellets before **(a)** and after **(b)** the post-annealing treatment. All the SPS's replica samples shows a dark and homogeneous black colour, while the post annealed samples show a light brownish colour. As reported by Malic et al., the dark colour of the SPS samples is related to the high concentration of oxygen vacancy and the consequent partial reduction of Nb^{5+} to Nb^{4+}.**[20]** This observation will be discussed in more detail later. In **Figure 2c** is reported the density of the samples.

The post annealing treatment causes a clear decrease of the density of the samples. The SA1 sample shows the highest density of 4.51 g/cm^3, which corresponds to the theoretical density of pure KNN. If we neglect the low concentration of bismuth and iron, it is reasonable to say that the sample is full dense (~ 100% of the theoretical density).**[21]** The SA2 and SA3 samples still maintain high density respectively of 4.48 g/cm^3 and 4.39 g/cm^3 while the SA4 and SA5 samples show lower density of about 4.19 g/cm^3. It is interesting to note that all the S1-5 samples exhibit very similar density values, close to the theoretical one, which confirms the high reproducibility and efficiency of this sintering method. Furthermore, it is evident that the density decreases up to a certain temperature around 1050°C, while a further increase of the post annealing temperature (1100°C) does not cause an additional change of the bulk density. In **Figure 3a** are reported the full XRD patterns of the sintered samples. The analysis carried out with the Rietveld method highlighted several structural complexities, which can be appreciated in much more details in **Figure 3b**. The convolution of the phases, that constitute the model used for the calculation, are indicated with different colour. The SA1 sample comes as a mixture mainly composed of an orthorhombic *Amm2* phase and a monoclinic *P1* KNN phase. It is often reported that the crystal structure of KNN is purely orthorhombic (s.g *Amm2*), or purely monoclinic (s.g *P1*). However, a recent work by Thong and co-workers has highlighted that the use of the monoclinic niobia polymorph leads to obtaining a heterogeneous product (see the calcined product in **Figure S1**).**[22]** In this case, it can be observed a similar situation where the main diffraction peaks are a mixture of two similar ferroelectric phases with different Na/K ratio, such as the orthorhombic *Amm2* phase and monoclinic *P1*, whose amount was estimated to be approximately equal to 32 and 67 wt.% (see **Table 1**). It is worth to point out that the fast-sintering rate, the low sintering temperature and the shorter soaking time of SPS process does not facilitate the homogenization of the different niobates at this stage. Moreover, the sintered sample contains some un-reacted bismuth and iron compounds in trace, which occur in their reduced form, most probably due to the reducing conditions of the SPS experiment. The SA2 sample has no secondary phases, this suggests that any residues have also reacted, volatilized or being absorbed in the matrix of the

perovskite following the annealing treatment. The best fit was obtained using the orthorhombic *Amm2* (68 wt.%) and the tetragonal *P4mm* (32 wt.%) phases, in agreement with other works.**[23]** From a comparison of the ionic radius, it is reasonable to expect that Bi^{3+} (103 pm) occupies the Na^{+} (102 pm) and K^{+} (138 pm) sites while Fe^{3+} (64.5 pm) occupies the Nb^{5+} (64 pm) sites. Both phases show large crystallinity (>2000 Å) which indicates that the post annealing treatment promotes the growth of grains. The samples treated at higher post annealing temperatures show similar crystal structure (SA3, SA4 and SA5), just only a slight increase of the Amm2 has been observed by increasing the post annealing temperature (**Table 1)**. Moreover, it should also be noted that the post-annealed samples do not contain any residues of polyniobate phase, which suggests that the volatility of the alkaline ions is negligible.**[24]**

In **Figure 4** are reported the Raman spectra of the samples. The Raman profile of KNN ceramics between 200-1000 cm^{-1} is attributable to internal vibrations, both stretching and bending modes, of the octahedral NbO_6 molecular group. Below 200 cm^{-1} all the signals are assigned to the translational modes of Na^{+}/K^{+} cations and rotation of the NbO_6 group.**[25-27]** The NbO_6 octahedron shows a cubic O_h symmetry and six normal vibrations:

$$\Gamma_{vib} = 1A_{1g}(\nu_1) + 1E_g(\nu_2) + 2F_{1u}(\nu_3, \nu_4) + 1F_{2g}(\nu_5) + 1F_{2u}(\nu_6) \quad (1)$$

Where, ν_1, ν_2 and ν_3 are stretching modes that involve Nb-O and O-Nb-O bonds while ν_4, ν_5 and ν_6 are bending modes of O-Nb-O bond.**[28]** The Raman spectra consists of three main signals, an asymmetric broad band between 200 and 300 cm^{-1} which consists of three contributions, related with the bending vibrations ν_4, ν_5 and ν_6. The second signal centred around at 620 cm^{-1} is also formed by three bands which correspond to the stretching vibrations ν_1, ν_2 and ν_3. Finally, the isolated band at 860 cm^{-1} is due to the $\nu_1 + \nu_5$ vibrational mode. At first glance, it emerges that the Raman scattering intensity of the annealed samples (SA2, SA3, SA4 and SA5) are much more intense than the fresh SPS sample (SA1). As reported in literature, the intensity of the Raman scattering is proportional to the grain size.**[29]** This evidence further confirms that the annealing treatment have caused an increase in the

size of grains. In order to provide a precise identification and assignment of Raman modes, the Raman spectra in the diagnostic range between 450 and 750 cm^{-1} have been analysed. The spectra have been fitted with two Lorenzian peaks (**Figure 5a-e**) that correspond to $A_{1g}(\nu_1)$ and $E_g(\nu_2)$ Raman modes, in agreement with Rubio-Marcos et al.**[30]** The peak of $A_{1g}(\nu_1)$ slight shift toward higher wavenumbers (**Figure 5f**) as the post annealing temperature increases. This behaviour is generally attributed to an increase in the force constant due to the shortening of the distance between the B-site atom and their coordinated oxygen. Therefore, this effect could be associated with the reduction of the oxygen vacancy concentration. As reported by Ceo et al., the evaluation of the FWHM of $A_{1g}(\nu_1)$ Raman mode can provide useful information as its reduction (sharpening of the peak) is correlated with the alleviation of the distortion of O-Nb-O angles and the increase in the interaction between Nb and O.**[31]** As shown in **Figure 5f,** it has been observed a strong reduction of FWHM value, in particular between the SA1 and SA2 samples, which further confirms that the Raman shift towards higher wavenumber it is due to a greater interaction between Nb and O.

In **Figure 6** are shown the SEM images of the fractured surface of the pellets. The SA1 sample (**Figure 6a**) reveals a highly dense microstructure which agrees with the experimental density measured. The annealed samples reveal a less dense microstructure characterized by an increase of porosity that seems to be related to the increase of the grain size with the annealing temperature. All the air annealed samples show a predominant transgranular fracture **(Figure 6a-d)** except for SA5 **(Figure 6e),** which is characterized by an intergranular fracture. This type of fracture generally happens due to weak bonding of the grains; therefore, it is reasonable to conclude that the post annealing treatment influences the grain growth and the bond between the particles which determines the transition from a transgranular to a predominant intergranular fracture for the highest air annealing temperature (1100°C).**[32] Figure 6(f)** of SO1 sample annealed in oxygen at 1050ºC for 2h shows the highest grain growth of all the annealed series, with exception of SA5. Furthermore, it can be highlighted the increase of porosity together with small pores in the grain boundaries and a drastic change from completely transgranular to intergranular fracture. This type of fracture reveals weakening of the grain

boundaries, when compared with SA3 and SA4 that also undergoes grain growth from SA1, most probably by oxygen vacancies migration to these. Comparison with SA4 (**Figure 6(d)**), indicates that the air annealing at the same temperature is less efficient to promote the grain growth of the SPS sample, but it does not produce a grain boundary degradation. In contrast, the short time annealing of SO2 keeps the previous density and a mixture of transgranular, mainly affecting the larger grains, and intergranular fractures (**Figure 6(g)**). Therefore, it shows that the grain boundaries are not so much altered by the treatment.

3.2 Electrical characterisation

The D.C resistance between the two silver electrodes of the SPS and annealed samples (Ø~14.5mm and t~1mm) was checked prior the electrical characterization. The SA1 sample showed relatively low resistance, in the order of few hundreds kΩ (~200 kΩ). As observed by other authors, this evidence can be explained by the high concentration of oxygen vacancy which makes the ceramic more conductive than the air sintered ones and thus, not suitable for poling and the electromechanical characterization.**[33]** In addition, it should also be considered the presence in trace of metallic bismuth and magnetite (**Figure 3a**) which could enhance this phenomenon. A clear improvement in terms of electrical resistance was achieved with the post-annealed samples. SA2, SA3 and SA4 showed similar values, in the order of few tens MΩ, while the resistance of SA5, SO1 and SO2 was found to be much larger (>50 MΩ). It is considered that the low resistivity should be closely related to the high concentration of point defects (oxygen vacancies) created during the processing.**[34]** In the present study, this effect is enhanced due to the reducing environment of SPS treatment which results in high amount of oxygen vacancies and the mentioned partial reduction of Nb^{5+} to Nb^{4+} in the perovskite structure.**[35]** At first glance, it appears that the annealing treatment has a positive effect on the insulating properties of KNN-BF, which seems to be correlated with the type of annealing and its temperature. To provide a deeper insight on the electrical behavior of the samples, the temperature dependence of the permittivity and dielectric losses were measured, and the results are shown in

Figure 7 and **Figure 8** respectively. Let us consider first the permittivity curves; all the ceramics present two clear dielectric anomalies, indicated as T1 and T2, that correspond to the orthorhombic-tetragonal (T1) and the tetragonal-cubic (T2) phase transitions between perovskite polymorphs. A slight difference in terms of phase transitions has been detected. SA2 and SA3 exhibit similar dielectric behavior and present T1 and T2 respectively at around 140 and 350 °C, while SA4 and SA5 show the same phase transitions at around 150 and 365°C respectively at 1 kHz. Therefore, the increase of the annealing temperature determines a shift towards higher temperatures of the dielectric anomalies. However, the biggest differences concern the magnitude of permittivity at high temperatures and the shape of the dielectric peaks. SA2 and SA3 are characterized by broad dielectric peaks and large permittivity around the Curie point; on the contrary, SA4 and SA5 are characterized by lower permittivity at high temperatures and sharper dielectric peaks (**Figure 7**). Noticeably, **Figure 7(e)** for SO1 annealed in oxygen for 1050ºC-2h reveals much lower frequency dependence than all samples of the air annealing series, making clear that the atmosphere for the annealing is of key importance.**[34-36]** Besides, the phase transitions at T_1 and T_2 are sharper. It is also evident the enhancement of the dielectric properties when compared to SA4 (**Figure 7(c)**), air annealed at the same temperature (1050ºC). **Figure 7(f)** for SO2 annealed in oxygen for 1050ºC-30 min also reveals a lower frequency dependence than all samples in the air annealed series. When results shown in **Figure 7(f)** are compared to both the SA3 curve before oxygen annealing (**Figure 7(b)**) and the one of SA4, air annealed at the same temperature (**Figure 7(b)**), the benefits of the oxygen annealing in reducing the concentration of points defects that promotes a lower frequency dependence became evident. **Figure 8** shows the dielectric losses as a function of the temperature. The SA2 sample shows high losses at low frequencies, as well as the SA3 sample which presents even higher losses at low frequencies and an increased frequency dependence. However, a change in trend was observed for the SA4 and SA5 samples who show a marked decrease in the high temperature dielectric losses with values comparable to those previously reported for air sintered KNN-BF ceramic.**[37]** In order to explain this behavior, it is necessary to consider two main contributions, which are the oxygen vacancy and the

microstructural features of the materials. As reported by Buscaglia et al., the grain size strongly affects the dielectric behavior of the ceramics.**[38]** In particular, ceramics characterized by small grain size typically show broad dielectric peaks which often causes a decrease of the Curie point. This observation perfectly fits with our experimental evidence. Regarding the behavior of the dielectric losses (**Figure 8**), it is widely accepted that oxygen vacancies are responsible for the A.C conduction mechanism in dielectric ceramics, which cause high dielectric losses, especially at high temperatures.**[39]** The formation of oxygen vacancy generates conducting electrons in perovskite structure oxides, written as follows (Equation 2):

$$O_O^X \rightarrow \frac{1}{2}O_2(g) + V_O^{\cdot\cdot} + 2e' \tag{2}$$

To explain the large dielectric permittivity (**Figure 7a-b**) and dielectric loss (**Figure 8a-b**) observed in the samples annealed at low temperatures (SA2 and SA3), it is necessary to consider the presence of the structural defects indicated in the equation expressed above. The generation of the double ionized oxygen vacancy is accompanied by the release of two electrons to keep the electric charge balance of the unit cell. When the external electric field and high temperature are applied, the electrons might deviate from the charge centre of $V_O^{\cdot\cdot}$. This phenomenon takes the name of *electron relaxation polarization* which determines the ultra-high dielectric constant and dielectric loss of the low-temperature annealed samples.**[40]** This behaviour is greatly reduced as the annealing temperature increases due to a better compensation of the oxygen vacancies. As a results, SA4 and SA5 presents lower permittivity and lower high-temperature dielectric losses. The SO1 sample, annealed at 1050ºC for 2h in oxygen flux, evidences the further efficiency of the oxygen annealing to reduce such effects, particularly when compared with the SA4 sample, annealed in air at the same temperature (**Figure 8(c)**). However, there are higher losses at low temperature than can be understood as a consequence of the microstructural degradation that this sample undergoes (**Figure 6(f)**). Overall, the less dispersive dielectric permittivity together with moderate losses are achieved when the SPS sample is treated with a combination of air annealing at a moderate temperature (1000ºC-2h) and a short treatment at a higher temperature in oxygen flux (1050ºC-30min). This follows the increase in grain size and an efficient

compensation of oxygen vacancies (**Figure 8(f)**), without the inconvenient weakening of the grain boundaries (**Figure 6(f)**).

In **Table 2** are reported the results of the electromechanical characterisation (Radial mode) of the samples poled at 20 kV/cm. The relatively low regression factor ($\Re^2$) of the recalculation to the experimental R and G curves, which is lower than expected in this mode resonance mode ($\Re^2$>0.99), is a consequence of small deviations from a circular shape of the samples and do not reflect a material property. However, it affects the results of the iterative method, leading to overestimation of the piezoelectric losses (underestimation of Q_p). In **Figure S2** are reported the equivalent plots of R and G, both the experimental and reconstructed peaks, used for the calculation of parameters of the samples with the automatic iterative method of the air and oxygen treated samples. From **Table 2** it clearly emerges that, among the air annealed samples, the best piezoelectric properties belong to those ones that have undergone a post-annealing treatment at 1000 (SA3) and 1050 °C (SA4). SA3 and SA4 show similar piezoelectric coefficients (d_{33} ~ 110 pC/N; d'_{31} ~ - 33 pC/N), coupling factor (k_p ~ 26 %) and RT permittivity at the planar resonance frequency (ε'^{T}_{33} ~ 477-506; tanδ ~ 0.06-0.07). The SA5 sample shows a deterioration of the electrical properties, i.e, lower piezoelectric coefficients and lower coupling factors but it has the highest mechanical quality factor (Q_m = 100) between the air annealed samples. In order to provide an explanation to this behaviour, it is necessary to consider the different microstructural features of the samples. As observed in **Figure 6**, the increase of the post annealing temperatures is accompanied by an increase in the size of the grains. It is well-known that the poling process is easier when the sizes of grains are large. The more complex domain configuration and the higher surface pinning of domain walls, result in higher energy needed for the reorientation of small grains.**[41]** Therefore, the best piezo coefficients of the samples SA3 and SA4 are related to the grain size increase. A further increase of the post annealing temperature (1100°C) determines a degradation of the microstructure, that is, lower density, higher porosity and weaker bond between the grains, which leads to lower piezoelectric coefficients. Although the SA3 and SA4 samples show good properties, these are lower than those obtained by air sintering reported in our previous work (d_{33} =

150 pC/N; k_p = 42%). Most likely, this is because the conduction mechanisms strongly reduce the sample resistance (**Table 2**), which decreases the actual voltage applied to the sample, affects the reorientation of the domains, and, therefore, the electromechanical properties of the ceramics.**[10]** The two samples annealed in oxygen stand the poling at 100ºC. Nevertheless, SO1 after oxygen annealing shows the lowest piezoelectric coefficient and coupling factor, the lowest RT permittivity at resonance, the highest dielectric losses and the lowest mechanical quality factor. The apparently high d_{33} is uncorrelated with the low parameters at resonance, also reflecting the degraded microstructure.**[42]** Notwithstanding the beneficial effect on the dielectric properties (**Figure 7(e)** and **Figure 8(e)**), the degradation of the microstructure (**Figure 6(f)**) results in low electromechanical performance. When comparing the properties of the SA3 and SO2, it is observed the enhancement of the dielectric elastic and electromechanical properties. The permittivity at resonance (ε'^{T}_{33}) increases and the dielectric loss (tanδ (ε^{T}_{33})) is the lowest of all samples analysed in this work. The directly calculated piezoelectric parameters (d_{33} = 117 pC/N, d'_{31}= -36.19 pC/N, k_p = 28%) undergo a moderate increase, both from those of SA3 and SA4, because of a more efficient poling, while the grain size changes very little in the short treatment in oxygen flow. The elastic stiffness (c'^{p}_{11} = 10.08 x 10^{10} N m^{-2}) decreases and the mechanical losses increases ($Q_m(c^{p}_{11})$ =140), being the best of all the studied samples and matching the values of the sample obtained by air sintering.**[10]** These results show how the SPS ceramics properties can be tailored by proper combination of annealing treatments in air and in oxygen flux and open a path for the knowledge-based optimization of the electrical and electromechanical properties of SPS KNN-based lead-free ceramics.

3.3 Toxicological assessment

To study the potential hazardous effects of the KNN-BF powders, the A549 cell line was used as model of human exposure, using a commercial PZT sample as benchmark. Thus, the viability of this cell line after being exposed during 24 h to different concentrations of the materials (6.4, 32, 160 mg/L), was determined by the neutral red uptake assay. **Figure 9** shows that none of the materials,

including the commercial PZT, caused a negative effect on the cell viability, presenting all the conditions similar percentages of viable cells than that observed in the control (non-exposed cells). The toxicological potential of these materials was also determined using the yeast *S. cerevisiae*, a widely used fungal model. In this case, this microorganism was exposed to 800 mg/L of the different materials for 24 hours, and their effect on the viability was evaluated through Colony Forming Units (CFUs) determination. **Figure 10** shows the results obtained. A statistically significant decrease was observed in the viability of cells exposed to SA1, SA2 and SA4, as well as in those exposed to the reference material. However, taking into account the high concentration used in the experiments and the reduction in this parameter observed (≤20 % in all the cases), the antifungal ability of the materials under study can be considered low.

The toxicity of KNN ceramics has been analysed in previous studies. Thus, due to their good biocompatibility, these materials were proposed as promising candidates for application in the development in implantable medical devices.**[43]** Regarding the safety of their powder forms, recently our group evaluated the toxicity of different KNNs with increasing amounts of $MgNb_2O_6$ ternary oxide in the same model organisms applied in this work.**[19]** The results described here using the A549 cells are in line with those obtained on the work cited above, since no effect on their viability was observed. On the other hand, the viability of *S. cerevisiae* was slightly decreased in presence of some of the materials under study here, suggesting that these specific KNN systems exhibit certain antifungal activity when they are present at high concentrations.

4. Conclusions

This work was dedicated to the processing optimization and the microstructural, electrical and cytotoxic characterization of the lead free ceramics with nominal composition $0.99K_{0.5}Na_{0.5}NbO_3$-$0.01BiFeO_3$ (KNN-BF) prepared by a combination of mechanochemical activation assisted synthesis and Spark Plasma Sintering. Attention was paid to the post annealing treatment. Results show that the annealing treatment causes important microstructural and electrical changes to the SPS sample. At the

same time, a decrease in the bulk density as a function of the annealing temperature has been observed. The untreated SPS sample is characterized by low electrical resistance, while the air annealed samples show better insulating properties due to a partial compensation of the oxygen vacancy, as confirmed by the Raman spectroscopy study. This effect would seem to improve as the annealing temperature increases. The best dielectric permittivity and electromechanical response is achieved when the SPS sample is treated with a combination of air annealing at a moderate temperature (1000ºC-2h) and a short treatment at a higher temperature in oxygen flux (1050ºC-30min). This follows both the most efficient grain growth of the as-SPS sample and the most efficient compensation of oxygen vacancies, without the inconvenient weakening of the grain boundaries resulting from air annealing at higher temperature (1100ºC-2h) or prolonged annealing in oxygen flux, even at lower temperature (1050ºC-2h). The toxicological tests carried out using both model organisms suggest that none of the materials is cytotoxic for the A549 human cell line. Regarding the experiments employing *S. cerevisiae*, certain antifungal activity was observed in the materials when this organism is exposed to them at high concentrations, being this effect similar to that observed in the PZT reference.

Acknowledgments

This work was partially supported by the Spanish MINECO R&D Project with ref. MAT-2017-86168R. The scholarship of A. Iacomini and M. Mureddu was supported by a joint agreement between Universities of Sassari and Cagliari (Italy) within the activities of the PhD programme in Chemical and Technological Sciences. The period spent by A. I. at the ICMM laboratories under the supervision of L. Pardo was made possible thanks to a generous support of the Erasmus+ programme. The authors are gratefully to Mireya Elisabet Pedrero, for her support in the toxicological assays. One of us, i.e. E. P., wishes to thank the Italian Ministry of Research for the project AIM 1815402-1 in the framework of PON R&I 2014-2020 – AIM (Attraction and International Mobility) where her activity is being performed. Fondazione di Sardegna is gratefully acknowledged for funding through “Bando

Fondazione di Sardegna 2022 e 2023 – Progetti di ricerca di base dipartimentali. All authors acknowledge the CeSAR (Centro Servizi d'Ateneo per la Ricerca) of the University of Sassari for the X-ray diffraction and SEM investigations.

References

[1] A. Vegas, M. Vallet-Regí, J. M. González-Calbet and M. A. Alario-Franco. The $ASnO_3$ (A=Ca,Sr) perovskites. *Acta Cryst*. B42 (1986) 167-172. https://doi.org/10.1107/S0108768186098403

[2] G.H Haertling, Ferroelectric Ceramics: History and Technology. *J. Am. Ceram. Soc*. 82(4) (1999) 797–818. https://doi.org/10.1111/j.1151-2916.1999.tb01840.x

[3] H. Fan and H.-E. Kim. Perovskite stabilization and electromechanical properties of polycrystalline lead zinc niobate–lead zirconate titanate. *J. Appl Phys.* 91 (2002) 317-322. https://doi.org/10.1063/1.1421036

[4] J. Shi, H.Q. Fan, X. Liu, Q. Li. Giant strain response and structure evolution in $(Bi_{0.5}Na_{0.5})0.945-x(Bi_{0.2}Sr_{0.7\square 0.1})xBa_{0.055}TiO_3$ ceramics. *J. Eur. Ceram. Soc.* 34 (2014) 3675-3683, https://10.1016/j.jeurceramsoc.2014.05.032

[5] S. Garroni, N. Senes, A. Iacomini, S. Enzo, G. Mulas, L. Pardo, S. Cuesta-Lopez, 2018. Advanced Synthesis on Lead-Free $K_xNa_{(1-x)}NbO_3$ Piezoceramics for Medical Imaging Applications. *Phys. Status Solidi A*. 215, 1700896. https://doi.org/10.1002/pssa.201700896

[6] J. Rödel, K. G.Webber, R. Dittmer, W. Jo, M. Kimura, D. Damjanovic. Transferring lead-free piezoelectric ceramics into application. *J Eur. Ceram. Soc*. 35(6) (2015) 1659-1681. https://doi.org/10.1016/j.jeurceramsoc.2014.12.013

[7] J. F. Li, K. Wang, F.-Y. Zhu, L.-Q. Cheng and F.-Z Yao. (K, Na)NbO_3-Based Lead-Free Piezoceramics: Fundamental Aspects, Processing Technologies, and Remaining Challenges. *J. Am. Ceram. Soc*. 96 (2013) 3677-3696. https://doi.org/10.1111/jace.12715

[8] A. Iacomini, S. Garroni, N. Senes, G. Mulas, S. Enzo, M. Poddighe, Á. García, J. F. Bartolomé, L. Pardo. $MgNb_2O_6$ Modified $K_{0.5}Na_{0.5}NbO_3$ Eco-Piezoceramics: Scalable Processing, Structural Distortion and Complex Impedance at Resonance. *ChemistryOpen*. 10 (2021) 798-805. https://doi.org/10.1002/open.202100089

[9] N. Senes, A. Iacomini, N. Domingo, S. Enzo, G. Mulas, S. Cuesta-Lopez, S. Garroni, S. (2018), Local Piezoelectric Behavior of Potassium Sodium Niobate Prepared by a Facile Synthesis via Water Soluble Precursors. *Phys. Status Solidi A* (2018) 215, 1700921. https://doi.org/10.1002/pssa.201700921

[10] A. Iacomini, S. Garroni, G. Mulas, S. Enzo, L. Cappai, M. Mureddu, C. Cau, Á. García, L. Pardo. Processing, phase evolution and electrical properties of "lead free" KNN–BF–CuO eco-piezoceramic from mechanochemically activated precursors. *Open Ceramics*. 9 (2022) 100247. https://doi.org/10.1016/j.oceram.2022.100247

[11] R. Pinho, A. Tkach, S. Zlotnik, M. E. Costa, J. Noudem, I. M.Reaney, P. M.Vilarinho. Spark plasma texturing: A strategy to enhance the electro-mechanical properties of lead-free potassium sodium niobate ceramics. *Appl. Mater Today.* 19 (2020) 100566. https://doi.org/10.1016/j.apmt.2020.100566

[12] F. Jean, F. Schoenstein, M. Zaghrioui, M. Bah, P. Marchet, J. Bustillo, F. Giovannelli, I. Monot-Laffez. Composite microstructures and piezoelectric properties in tantalum substituted lead-free $K_{0.5}Na_{0.5}Nb_{1-x}TaxO_3$ ceramics. *Ceram Int*. 44 (2018) 9463–9471. https://doi.org/10.1016/j.ceramint.2018.02.163

[13] I. Monot-Laffez, R. Retoux, M. Zaghrioui, M. Bah, M. Dubernet, F. Dorvaux, F. Delorme, F. Giovannelli . Microstructural features and piezoelectric properties of spark plasma sintered lead-free $K_{0.5}Na_{0.5}NbO_3$ ceramics. *Eur. Phys. J. Spec. Top*. (2022). https://doi.org/10.1140/epjs/s11734-022-00573-y

[14] Y. Zhen, J.F. Li, K. Wang, Y. Yan, L. Yu. Spark plasma sintering of Li/Ta-modified (K,Na)NbO_3 lead-free piezoelectric ceramics: Post-annealing temperature effect on phase structure, electrical properties and grain growth behavior. *Mater Sci Eng B.* 176 (2011) 1110–1114. https://doi.org/10.1016/j.mseb.2011.05.051

[15] M. Dubernet, M. J. Pitcher, M. Zaghrioui, M, Baha, J. Bustillo, F. Giovannelli, I. Monot-Laffez. Synthesis routes for enhanced piezoelectric properties in spark plasma sintered Ta-doped KNN ceramics. *J. Eur Ceram. Soc.* 42(5) (2022) 2188-2194. https://doi.org/10.1016/j.jeurceramsoc.2021.12.030

[16] M. Jiang, X. Liu, and G. Chen. Phase structures and electrical properties of new lead-free $Na_{0.5}K_{0.5}NbO_3$–$LiSbO_3$–$BiFeO_3$ ceramics *Scr. Mater.* 60 (2009) 909-912. https://doi.org/10.1016/j.scriptamat.2009.02.017

[17] C. Alemany, A. M. González, L. Pardo, B. Jiménez, F. Carmona, & J. Mendiola. Automatic determination of complex constants of piezoelectric lossy materials in the radial mode *J. Phys. D.* 28(5) (1995) 945–956. https://doi.org/10.1088/0022-3727/28/5/017

[18] L. Pardo, A. García, F Schubert, A. Kynast, T. Scholehwar, A. Jacas and J. F. Bartolomé. "Determination of the PIC700 Ceramic's Complex Piezo-Dielectric and Elastic Matrices from Manageable Aspect Ratio Resonators". Materials, 14 (15), 4076 (2021). https://doi.org/10.3390/ma14154076

[19] A. Iacomini, J. A. Tamayo-Ramos, C. Rumbo, I. Urgen, M. Mureddu, G. Mulas, S. Enzo, S. Garroni. Processing Optimization and Toxicological Evaluation of "Lead-Free" Piezoceramics: A KNN-Based Case Study. *Materials.* 14(15) (2021) 4337. https://doi.org/10.3390/ma14154337.

[20] D. Kuscer, A. Kocjan, M. Majcen, A. Meden, K. Radan, J. Kovač, B. Malič. Evolution of phase composition and microstructure of sodium potassium niobate –based ceramic during pressure-less

spark plasma sintering and post-annealing. *Ceram Int*. 45 (2019) 10429–10437. https://doi.org/10.1016/j.ceramint.2019.02.102

[21] H. Birol, D. Damjanovic, N. Setter. Preparation and characterization of $(K_{0.5}Na_{0.5})NbO_3$ ceramics *J. Eur. Ceram. Soc*. 26 (2006) 861–866. https://doi.org/10.1016/j.jeurceramsoc.2004.11.022

[22] H.-C. Thong, C. Zhao, Z.-X. Zhu, X. Chen b, J.-F. Li, K. Wang. The impact of chemical heterogeneity in lead-free (K, Na)NbO_3 piezoelectric perovskite: Ferroelectric phase coexistence *Acta Mater*. 166 (2019) 551-559. https://doi.org/10.1016/j.actamat.2019.01.012

[23] A. Khesro, D. Wang, F. Hussain, R. Muhammad, G. Wang, A. Feteira, and I. M. Reaney. Temperature Dependent Piezoelectric Properties of Lead-Free $(1\text{-}x)K_{0.6}Na_{0.4}NbO_3$–$xBiFeO_3$ Ceramics. *Front. Mater*. 7 (2020) 140. https://doi.org/10.3389/fmats.2020.00140

[24] F. Hussain, I. Sterianou, A. Khesro, D. C. Sinclair, and I. M. Reaney. p-type/n-type behaviour and functional properties of KxNa(1-x)NbO3 (0.49<x<0.51) sintered in air and N2. *J. Eur. Ceram. Soc*. 38(9) (2018) 3118-3126. https://doi.org/10.1016/j.jeurceramsoc.2018.03.013

[25] M. Polomska, B. Hilczer, M. Kosec, & B. Malič. Raman Scattering Studies of Lead Free $(1\text{-}x)K_{0.5}Na_{0.5}NbO_3$-$xSrTiO_3$ Relaxors. *Ferroelectrics*. 369(1) (2008) 149–156. https://doi.org/10.1080/00150190802374873

[26] R. Singh, K. Kambale, A. R. Kulkarni, C. S. Harendranath. Structure composition correlation in KNN–BT ceramics – An X-ray diffraction and Raman spectroscopic investigation. *Mater. Chem. Phys*. 138(2–3) (2013) 905–908. https://doi.org/10.1016/j.matchemphys.2012.12.082

[27] L. Liu, M. Knapp, H. Ehrenberg, L. Fang, H. Fan, L.A. Schmitt, H. Fuess, M. Hoelzel, H. Dammak, M.P. Thi, M. Hinterstein. Average vs. local structure and composition-property phase diagram of $K_{0.5}Na_{0.5}NbO_3$-$Bi_{½}Na_{½}TiO_3$ system. *J. Eur. Ceram. Soc.* 37 (2017) 1387-1399. https://doi.org/10.1016/j.jeurceramsoc.2016.11.024

[28] W. L. Zhu, J. L. Zhu, Y. Meng, M. S. Wang, B. Zhu, X. H. Zhu, J. G. Zhu, D. Q. Xiao, G. Pezzotti. Structural characteristics of Mg-doped (1-x)($K_{0.5}Na_{0.5}$)NbO_3–x$LiSbO_3$ lead-free ceramics as revealed by Raman spectroscopy. *J. Phys. D: Appl. Phys.* 44 (2011) 505303. https://doi.org/10.1088/0022-3727/44/50/505303

[29] Y. L. Du, M. S. Zhang, Q. Chen, Z. Yin. Investigation of size-driven phase transition in bismuth titanate nanocrystals by Raman spectroscopy. *Appl. Phys. A.* 76 (2003) 1099–1103. https://doi.org/10.1007/s00339-002-1950-2

[30] F. Rubio-Marcos, M. A. Banares, J. J. Romero and J. F. Fernandez. Correlation between the piezoelectric properties and the structure of lead-free KNN-modified ceramics, studied by Raman Spectroscopy. *J. Raman Spectrosc*. 42 (2011) 639–643. https://doi.org/10.1002/jrs.2753

[31] Z. Cen, X. Wang, Y. Huan, L. Li. Temperature stability and electrical properties of MnO-doped KNN-based ceramics sintered in reducing atmosphere. *J Am Ceram Soc*. 101 (2018) 2391–2407. https://doi.org/10.1111/jace.15411

[32] D. Liu, H. Du, F. Tang, F. Luo, D. Zhu, W. Zhou. Effect of heating rate on the structure evolution of ($K_{0.5}Na_{0.5}$)NbO_3–$LiNbO_3$ lead-free piezoelectric ceramics. *J. Electroceram*. 20 (2008) 107–111. https://doi.org/10.1007/s10832-007-9373-2

[33] M. Bah, F. Giovannelli, F. Schoenstein, G. Feuillard, E. LeClezio, I. Monot-Laffez. High electromechanical performance with spark plasma sintering of undoped $K_{0.5}Na_{0.5}NbO_3$ ceramics *Ceram. Int.* 2014, 40(5), 7473–7480. https://doi.org/10.1016/j.ceramint.2013.12.097

[34] C. Long, T. Li, H. Fan, Y. Wu, L. Zhou, Y. Li, L. Xiao, Y. Li. Li-substituted $K_{0.5}$ $Na_{0.5}NbO_3$-based piezoelectric ceramics: crystal structures and the effect of atmosphere on electrical properties. *J. Alloy. Compd.* 658 (2016) 839-847. https://doi.org/10.1016/j.jallcom.2015.10.245

[35] Y. Huan, X. Wang, T. Wei, J. Xie, Z. Ye, P. Zhao, L. Li. Defect engineering of high-performance potassium sodium niobate piezoelectric ceramics sintered in reducing atmosphere. *J Am Ceram Soc.* 100 (2017) 2024–2033. https://doi.org/10.1111/jace.14721

[36] H. Fan, G. Park, J. Choi, J. Ryu, H. Kim. Preparation and Improvement in the Electrical Properties of Lead-zinc-niobate–based Ceramics by Thermal Treatments. *J Mater Res.* 17(1) (2002) 180-185. https://doi.org/10.1557/JMR.2002.0027

[37] R. Zuo, C. Ye, X. Fang. $Na_{0.5}K_{0.5}NbO_3$–$BiFeO_3$ lead-free piezoelectric ceramics *J. Phys. Chem. Sol*. 69 (2008) 230–235. https://doi.org/10.1016/j.jpcs.2007.08.066

[38] V. Buscaglia, M.T. Buscaglia, M. Viviani, L. Mitoseriu, P. Nanni, V. Trefiletti, P. Piaggio, I. Gregora, T. Ostapchuk, J. Pokorny´, J. Petzelt. Grain size and grain boundary-related effects on the properties of nanocrystalline barium titanate ceramics. *J. Eur Ceram Soc*. 26 (2006) 2889–2898. https://doi.org/10.1016/j.jeurceramsoc.2006.02.005

[39] T.-F.Zhang, X.-G. Tang, Q.-X. Liu, Y.-P. Jiang, X.-X. Huang. Oxygen-Vacancy-Related High Temperature Dielectric Relaxation in $(Pb_{1-x}Ba_x)ZrO_3$ Ceramics. *J. Am. Ceram. Soc*. 98 (2015) 551-558. https://doi.org/10.1111/jace.13317

[40] B. Wang, F. Liu, F. Zhang, G. Chen, Z. Liu, Y. Li. Effects of the post-annealing reductive-atmosphere-sintered $(K_{0.48}Na_{0.52})NbO_3$ lead-free piezoceramics. *Ceram. Int*. 46(17) (2020) 27373-27380. https://doi.org/10.1016/j.ceramint.2020.07.222

[41] R.-A. Eichel, E. Erünal, P. Jakes, S. Körbel, C. Elsässer, H. Kungl, J. Acker, M. J. Hoffmann. Interactions of defect complexes and domain walls in CuO-doped ferroelectric $(K,Na)NbO_3$. *Appl. Phys. Lett*. 102 (2013) 242908. https://doi.org/10.1063/1.4811268

[42] J. Mendiola, C. Alemany, L. Pardo, A. Gonzalez. Poling reversal effects on piezoelectricity of calcium modified lead titanate ceramic. *Ferroelectrics.* 94 (1989) 209-214. https://doi.org/10.1080/00150198908014255

[43] N. H. Gaukås, Q.-S. Huynh, A. A. Pratap, M.-A. Einarsrud, T. Grande, R. M. D. Holsinger and J. Glaum. In Vitro Biocompatibility of Piezoelectric $K_{0.5}Na_{0.5}NbO_3$ Thin Films on Platinized Silicon Substrates. *ACS Appl. Bio Mater*. 3(12) (2020) 8714–8721. https://doi.org/10.1021/acsabm.0c01111

Images

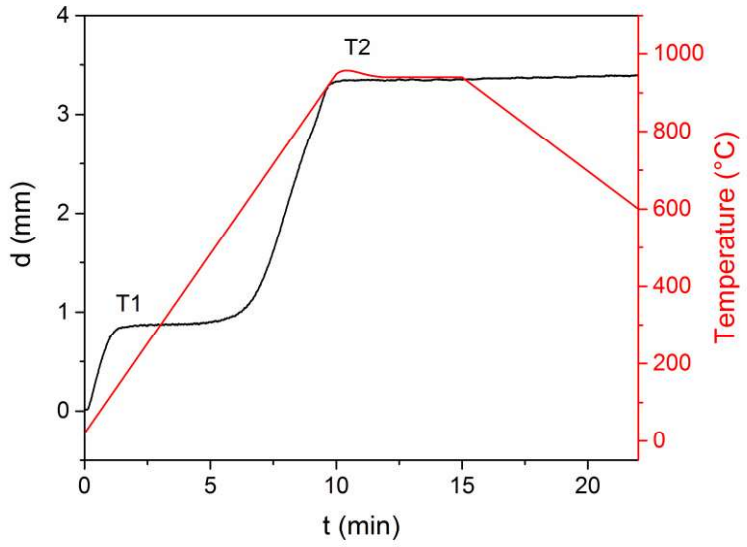

Figure 1. Temperature and sample displacement (d) of KNN-BF sample during the SPS process.

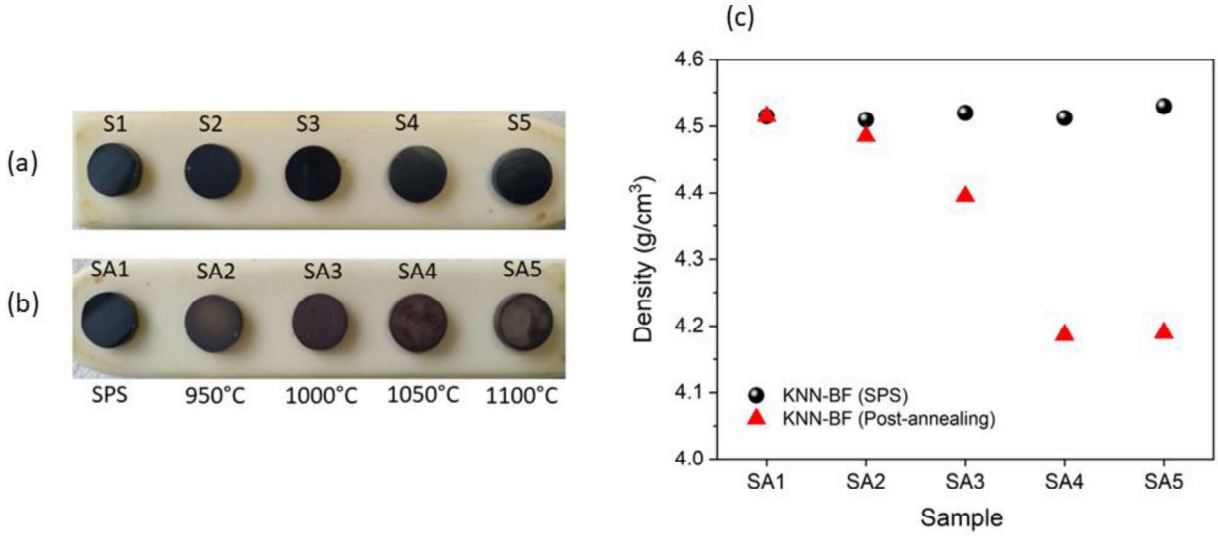

Figure 2. Photographs of KNN-BF pellets obtained through Spark Plasma Sintering (a) before and (b) after the post-annealing process. Labels under the post annealed samples indicated the post annealing temperatures. (c) Density of the samples before (black) and after (red) the post annealing treatment.

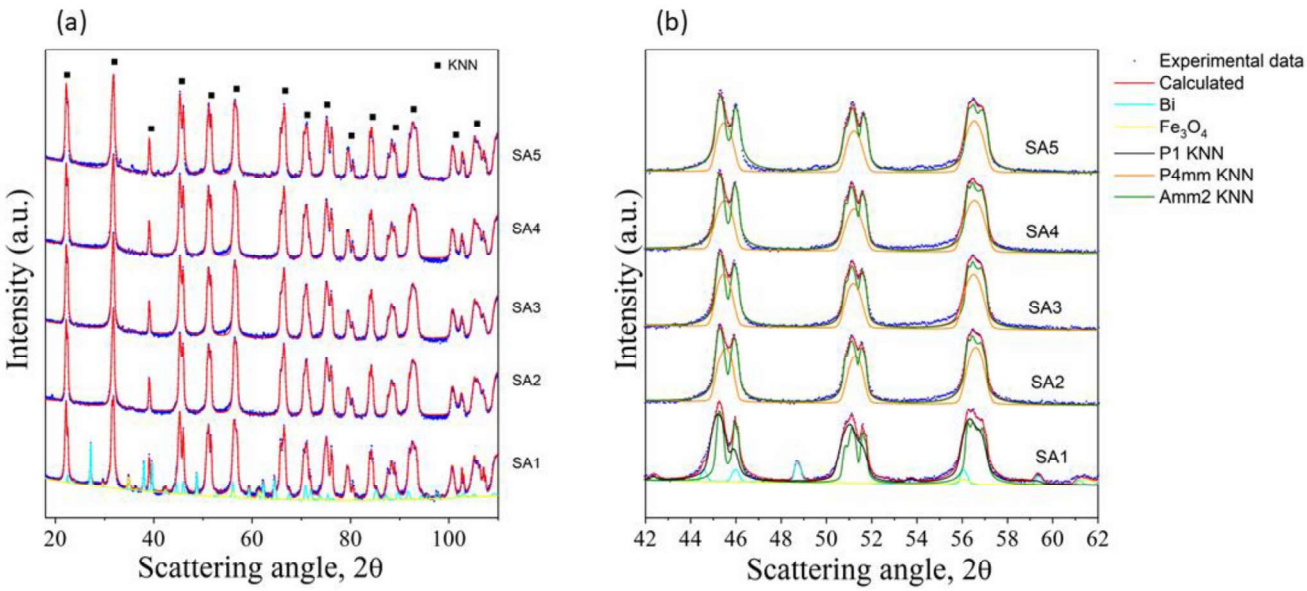

Figure 3. (a) XRD patterns (log scale) of KNN-BF samples. Blue dots represent the experimental data. Red curve is the calculated fit obtained from the sum of the phases used as a model in the calculation. The Cyan and yellow curves belong to the secondary phases identified in the SA1 samples, which are respectively bismuth and magnetite. (b) Magnification of some diagnostic peaks between 42 and 62°C. Different colour lines indicate the phases used in the model.

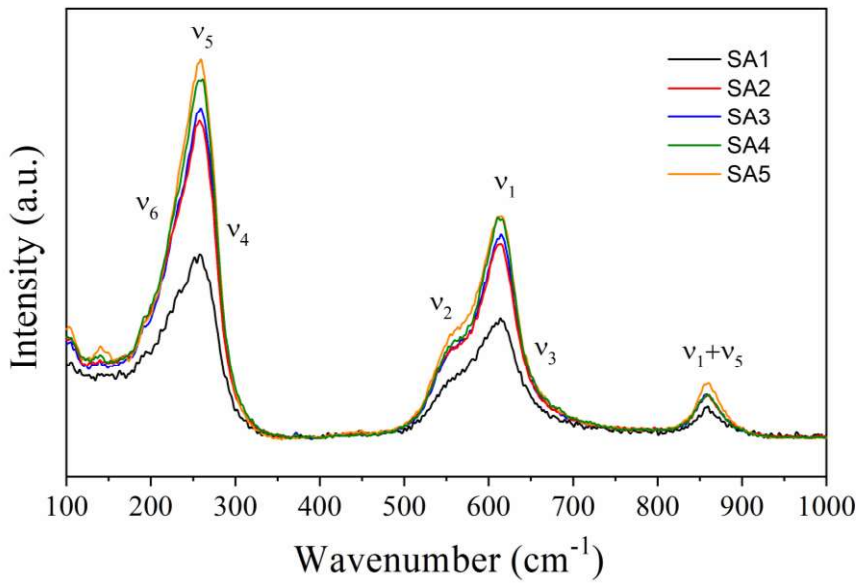

Figure 4. Room temperature Raman spectra of KNN-BF samples.

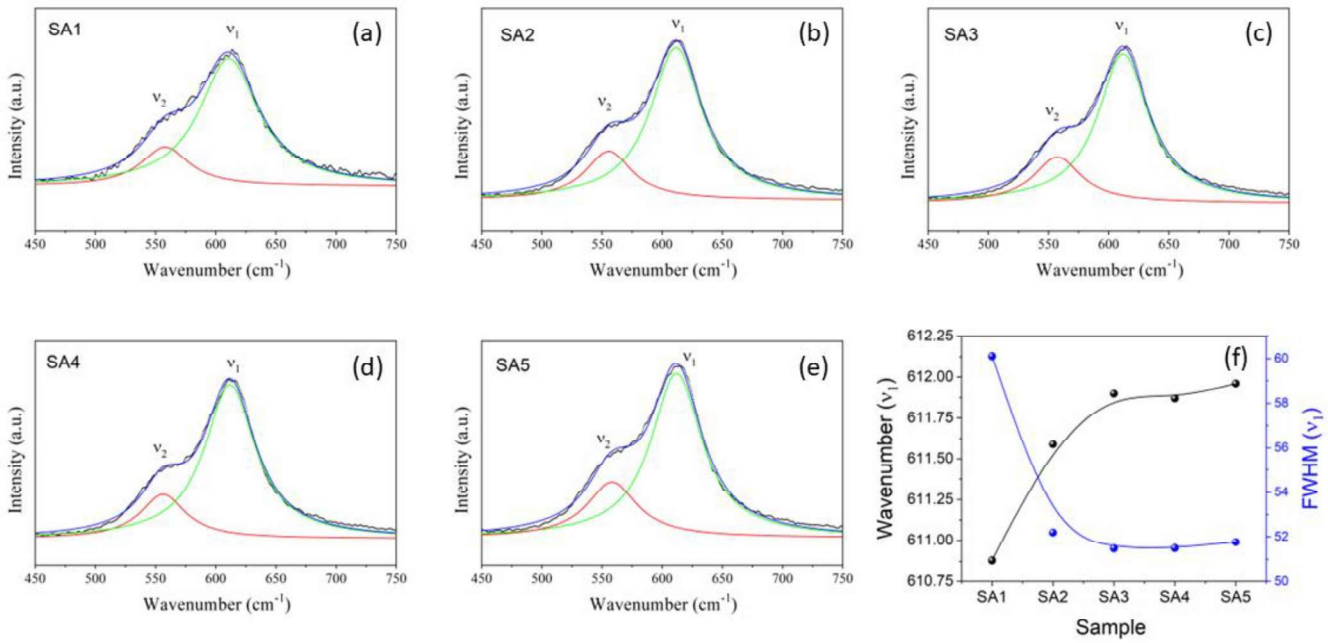

Figure 5. (a-e) Raman spectra of the SPS samples in the wavenumber range between 450 and 750 cm^{-1} and Lorenzian fit of the $A_{1g}(\nu_1)$ (green lines) and $E_g(\nu_2)$ (red lines). (b) Evolution of the wavenumber and FWHM of $A_{1g}(\nu_1)$ Raman modes as a function of the post annealing temperature, expressed here with the corresponding sample label.

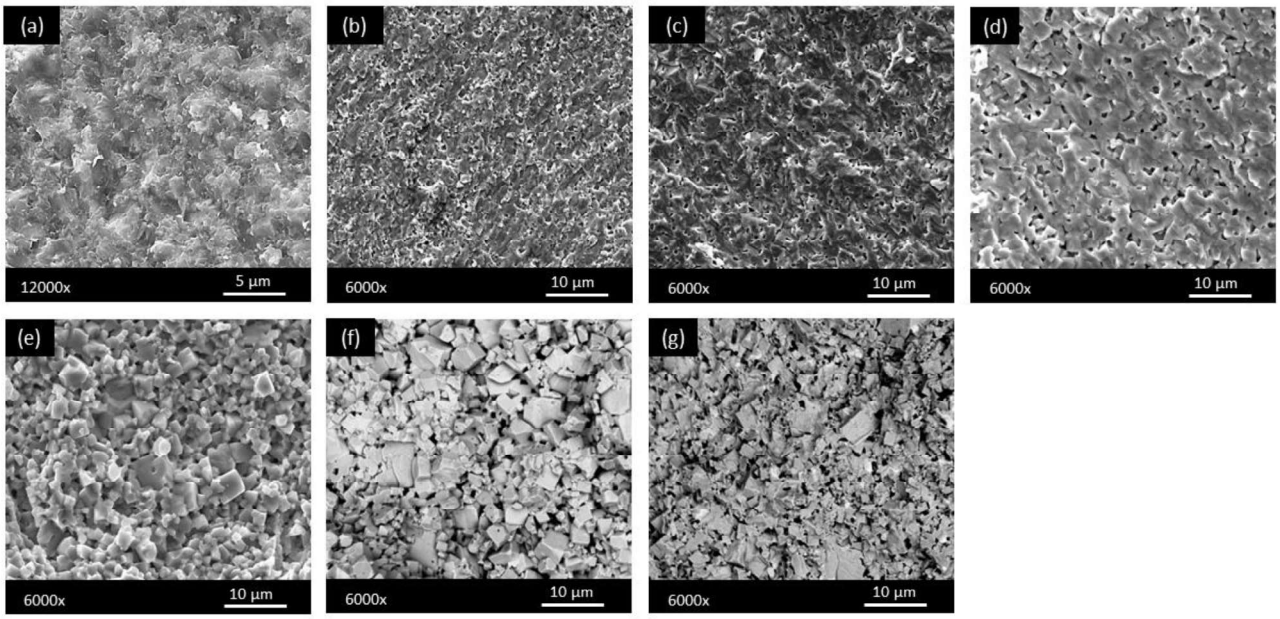

Figure 6. Fractured surface images of sintered pellets. (a) SA1, (b) SA2, (c) SA3, (d) SA4, (e) SA5, (f) SO1 and (f) SO2. Please note the different magnification for the SA1 sample.

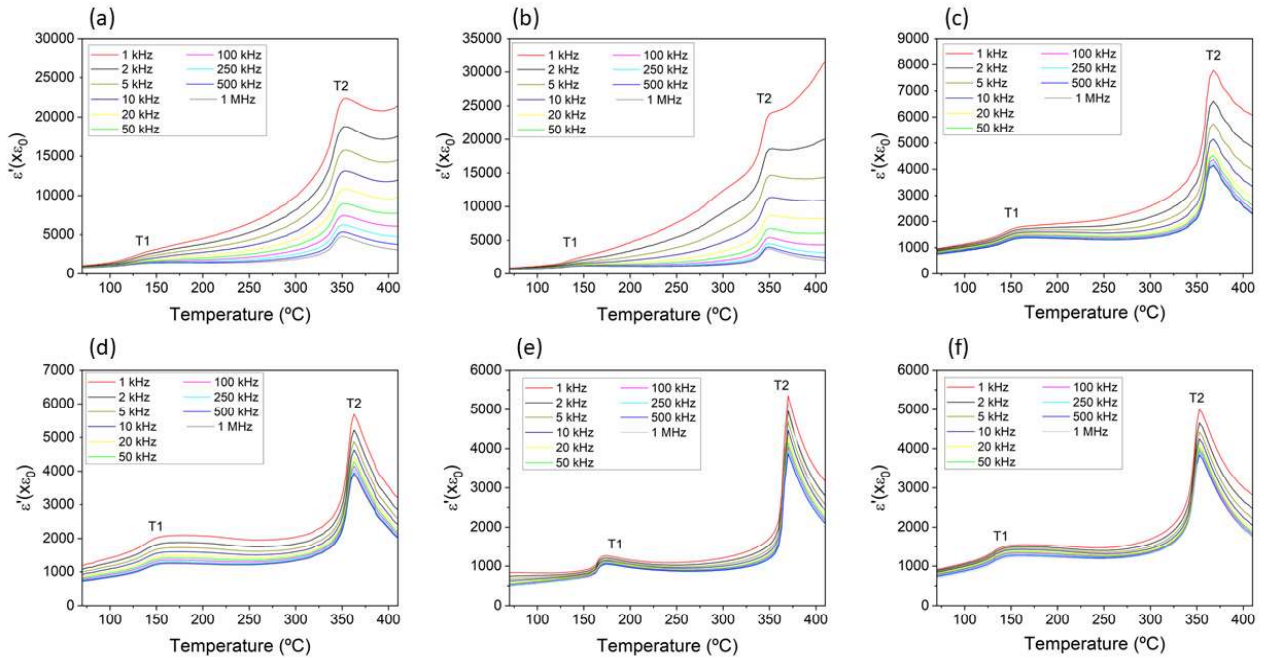

Figure 7. Dielectric permittivity ε^{T}_{33} vs. temperature for (a) SA2, (b) SA3, (c) SA4, (d) SA5, (e) SO1 and (f) SO2.

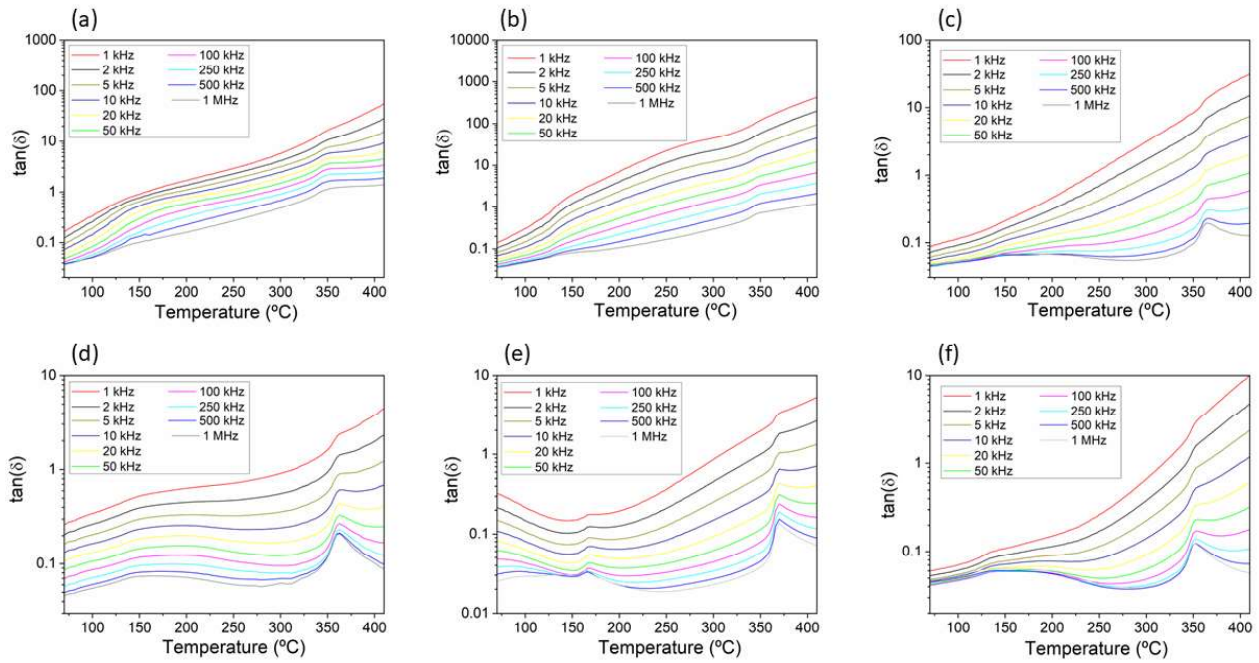

Figure 8. Dielectric losses (log scale) tanδ vs. temperature for (a) SA2, (b) SA3, (c) SA4, (d) SA5, (e) SO1 and (f) SO2.

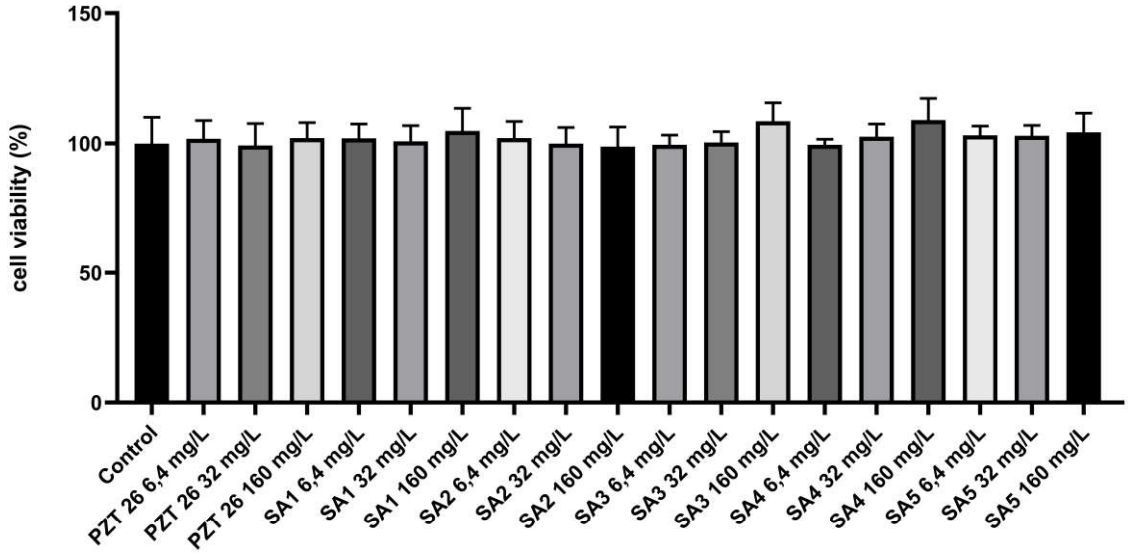

Figure 9. Viability of A549 cells (neutral red assay) after exposure to different concentrations of piezoelectric materials. Results are expressed as % of control (cells in the absence of materials). Data represent the mean of at least 5 biological replicates obtained in 2 independent experiments ± standard deviation, SD. Differences were established using a one-way ANOVA followed by a Dunnet *post hoc* test to compare each mean to the control, and were considered significant at $P \leq 0.05$.

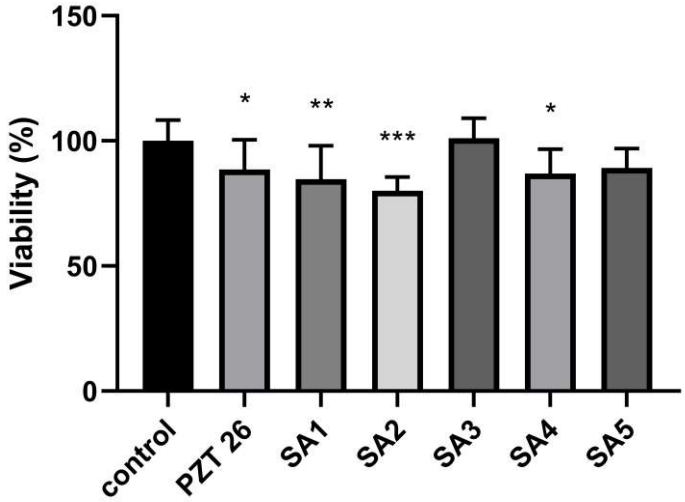

Figure 10. Colony forming units (CFUs) of *S. cerevisiae* cells exposed to 800 mg/L of the piezoelectric materials. Results are expressed as the percentage (%) of CFUs determined for each exposure condition using as reference value the non-exposed cells condition, which was assigned a

value of 100%. Data represent the mean of at least 5 biological replicates obtained in 3 independent experiments ± standard derivation, SD. Differences were established using a one-way ANOVA followed by a Dunnet *post hoc* test to compare each mean to the control, and were considered significant at $P \leq 0.05$. $*P \leq 0.05$, $**P \leq 0.01$, $***P \leq 0.001$.

Tables

Sample	Phase (s.g)	a (Å)	b (Å)	c (Å)	V (Å^3)	Cryst. Size (Å)	wt. %	R_{wp} (%)
SA1	*Amm2*	3.9467	5.6447	5.6796	126.530	889	32	8.48
	P1	5.6687	3.9531	5.6729	127.124	1029	67	
	Fd-3m (Fe_3O_4)	8.5258	8.5258	8.5258	619.734	709	<1	
	R-3m (Bi)	4.5462	4.5462	11.8600	245.122	1839	<1	
SA2	*Amm2*	3.9509	5.6471	5.6769	126.658	>2000	68	10.02
	P4mm	3.9771	3.9771	3.9994	63.260	>2000	32	
SA3	*Amm2*	3.9502	5.6457	5.6762	126.588	>2000	69	9.50
	P4mm	3.9772	3.9772	3.9944	63.184	>2000	31	
SA4	*Amm2*	3.9483	5.6471	5.6787	126.615	>2000	71	9.62
	P4mm	3.9806	3.9806	4.0025	63.420	>2000	29	
SA5	*Amm2*	3.9452	5.6447	5.6752	126.384	>2000	71	14.69
	P4mm	3.9729	3.9729	3.9999	63.134	>2000	29	

Table 1. Crystallographic information obtained from Rietveld refinement of SPS's samples. The β angle of the monoclinic P1 cell of Sh1 sample is 90.04°.

Properties /Sample	SA2	SA3	SA4	SA5	SO1	SO2
$\Re^2$	0.968	0.987	0.995	0.999	0.927	0.978
d_{33} (pC/N)	73	110	109	55	86	117
d'_{31} (pC/N)	-26.69	-32.27	-32.79	-19.56	-8.92	-36.19
$Q_p(d_{31})$	46	94	416	25	17	66
k_p (%)	20	26	25	15	8	28
ε'^{T}_{33}	573	477	506	532	375	515
tanδ	0.046	0.061	0.076	0.064	0.093	0.043
c'^{p}_{11} (10^{10}N m^{-2})	11.35	11.34	11.52	10.43	10.69	10.08
Q_m	93	69	79	100	64	140

Table 2. Some relevant material coefficients obtained from the Radial mode of resonance of KNN-BF ceramics obtained by Spark Plasma Sintering method. The complex material coefficients (P=P′+iP′′) are given as real part (P′) and losses (piezoelectric and mechanical Q factor (P′/P′′) and dielectric tanδ (P′′/P′)).